ACS APPLIED ENERGY MATERIALS

Subscriber access provided by Brought to you by CSIR Information Services

Article

Dual Polymer/Liquid Electrolyte with BaTiO3 Electrode for Magnesium Batteries

Eslam Sheha, Fanfan Liu, Tiantian Wang, Mohamed Farag, Junnan Liu, Nasser Yacout, Mesfin Kebede, Neeraj Sharma, and Li-Zhen Fan

ACS Appl. Energy Mater., **Just Accepted Manuscript** • Publication Date (Web): 29 Apr 2020

Downloaded from pubs.acs.org on April 30, 2020

Just Accepted

"Just Accepted" manuscripts have been peer-reviewed and accepted for publication. They are posted online prior to technical editing, formatting for publication and author proofing. The American Chemical Society provides "Just Accepted" as a service to the research community to expedite the dissemination of scientific material as soon as possible after acceptance. "Just Accepted" manuscripts appear in full in PDF format accompanied by an HTML abstract. "Just Accepted" manuscripts have been fully peer reviewed, but should not be considered the official version of record. They are citable by the Digital Object Identifier (DOI®). "Just Accepted" is an optional service offered to authors. Therefore, the "Just Accepted" Web site may not include all articles that will be published in the journal. After a manuscript is technically edited and formatted, it will be removed from the "Just Accepted" Web site and published as an ASAP article. Note that technical editing may introduce minor changes to the manuscript text and/or graphics which could affect content, and all legal disclaimers and ethical guidelines that apply to the journal pertain. ACS cannot be held responsible for errors or consequences arising from the use of information contained in these "Just Accepted" manuscripts.

is published by the American Chemical Society. 1155 Sixteenth Street N.W., Washington, DC 20036

Published by American Chemical Society. Copyright © American Chemical Society. However, no copyright claim is made to original U.S. Government works, or works produced by employees of any Commonwealth realm Crown government in the course of their duties.

Dual Polymer/Liquid Electrolyte with $BaTiO_3$ Electrode for Magnesium Batteries

Eslam Sheha*[1], Fanfan Liu[2], Tiantian Wang[2], Mohamed Farrag[1], Junnan Liu[3], Nasser Yacout[1], Mesfin A Kebede[4], Neeraj Sharma[3], Li-Zhen Fan[2]

[1]Physics Department, Faculty of Science, Benha University,13518, Benha, Egypt

[2]Beijing Advanced Innovation Center for Materials Genome Engineering, Beijing Key Laboratory for Advanced Energy Materials and Technologies, University of Science and Technology Beijing, Beijing 100083, China

[3]School of Chemistry, The University of New South Wales, Sydney, Australia

[4]Energy Centre, Council for Scientific and Industrial Research (CSIR), Pretoria, 0001, South Africa

Abstract With a low cost and high volumetric capacity, rechargeable magnesium batteries (RMBs) have emerged as promising candidates for post-lithium ion batteries. The kinetically sluggish Mg^{2+} insertion/extraction in the host lattice and the anode/electrolyte incompatibility render the battery irreversible in some instances and restrict the commercial applications. In this work, we replace the conventional electrolyte with a dual layer of liquid and polymer electrolyte onto the cathode and anode, respectively, and investigate the structure, electrical and electrochemical properties. It exhibits a remarkable Mg-ion conductivity up to 4.62×10^{-4} S cm^{-1} at 55 ºC, a high transfer number ($t_{Mg^{2+}}$ = 0.74), low over potential and relatively stable Mg stripping and plating during the initial cycles. Furthermore, this work uses an unconventional electrode, $BaTiO_3$ (BTO), to demonstrate the performance of Mg batteries, and track the structural and electrochemical changes. The quasi-solid-state Mg batteries fabricated with pre-magnesiation and thermal treated BTO cathode materials show good electrochemical performance. The approaches herein may provide new directions for exploiting high-performance Mg batteries through the perovskite structure cathode and functional dual electrolyte.

Keywords: composite polymer electrolyte; magnesium ion battery; dual electrolyte; $BaTiO_3$; ferroelectric transition.

Introduction

Lithium-ion batteries (LIBs) with high energy density have received widespread attention and have shown significant developments in the past few decades. However, they still face many challenges, such as high prices, scarcity of resources and safety issues. It is predicted that LIBs might not be able to meet the needs of road transport electrification in the near future[1]. Rechargeable magnesium batteries (RMBs), as a sustainable energy storage system, have recently attracted attention as a beyond lithium battery owing to the low price of magnesium, potential stability in air, high theoretical volumetric capacity (~ 3833 mAh cm^{-3} vs 2062 mAh cm^{-3} for Li) and the low reduction potential (-2.4 V vs. SHE)[2-3]. Despite these positive features, there are two major challenges that need to be overcome before realizing practical RMBs. First, unlike the LIBs, magnesium forms a "truly" passivating film in contact with oxygen or conventional electrolytes which impede Mg^{2+} transfer. Therefore, RMBs require an ideal electrolyte in which no "solid electrolyte interphase" (SEI) or a weakened passivation layer is formed on the Mg metal surface to enable highly reversible Mg plating/stripping[4]. In addition, the strong polarization of divalent Mg^{2+} ions results in sluggish diffusion kinetics of Mg^{2+} in host materials [5], and it is therefore necessary to design a cathode material that permits the Mg^{2+} reversible insertion/extraction with relatively fast kinetics. In order to solve these problems, in this paper, we try to exploit new approaches to overcome these challenges.

Developing an electrolyte, which can be compatible with the Mg metal anode, mitigating formation of the passivation layer that occurs in the presence of trace impurities, water, and certain solvents/salts, is still one of the intractable challenges to realize a practical Mg battery. There are

strategies that have been adopted to exploit Mg electrolytes capable of reversible Mg deposition and overcome this problem so far. For instance, taking advantage of the strong reductive nature of $Mg(BH_4)_2$ and Grignard reagents that act as scavengers for reducible species in electrolyte solutions[6-7]. However, this and other similar strategies reported to date do not entirely meet the criteria for an ideal electrolyte with low cost, ease of preparation, halogen free, sustainable, non-volatile, non-hazardous and low flammability. Moreover, based on the potential of the lowest unoccupied molecular orbital (LUMO) and the highest unoccupied molecular orbital (HOMO), for an ideal electrolyte in RMBs, the potential of the LUMO should be higher than the Fermi level of anode, while the HOMO should be lower than the Fermi level of cathode[8]. So, this can be achieved by adjusting the position of the LUMO and HOMO levels at the interface of Mg/electrolyte and electrolyte/cathode to decrease electrolyte reduction on the anode and oxidation on the cathode [9]. The strategy of replacing the conventional electrolyte with an alternative dual electrolyte may be the alternative approach to overcome the incompatibility of LUMO and HOMO energy levels positions. Gel polymer electrolytes (GPEs) become a promising alternative for solid and liquid polymer electrolytes due to its high conductivity along with good mechanical strength, flexibility, good interface stability and better manufacturing integrity. Recently, many research works have studied GPEs doped with magnesium salts and blended with different host polymers such as polyethylene oxide (PEO)[10] polymethylmethacrylate (PMMA)[11], polyvinylidenefluoride (PVdF)[12], and polyvinylidenefluoride-hexafluoropropylene (PVdF-HFP)[13]. Among these systems, PVdF is the most commonly used polymer host in GPEs, the PVdF-based GPEs have received significant attention due to the VdF unit which provides the structural integrity to support freestanding film formation. In addition, the PVdF-based GPEs possess good mechanical properties, and thermal and chemical stability. Hence, PVdF was chosen as the polymer host for the synthesis of the polymer electrolyte in this work.

BTO has a tetragonal crystal structure at room temperature and belongs to the perovskite family, however when the temperature exceeds 120 ^{o}C, it transforms from the ferroelectric tetragonal phase to paraelectric cubic phase[14] in a centro-symmetric space group that results in zero net polarization and thus no ferroelectricity[15]. Importantly, to the best of our knowledge, no research has been conducted on the effect of interaction between alkali ion insertion mechanism and the electrochemical performance of BTO electrodes. This motivates us to shed some light over this issue.

Based on the above discussion, the development of Mg ion-conducting electrolytes has become one of the important issues to realize quasi-solid-state magnesium batteries. In the present study, a polymer electrolyte film of PVdF, tetraethylene glycol dimethyl ether and magnesium trifluoromethanesulfonate ($Mg(CF_3SO_3)_2$) SPE is prepared by using the solution casting technique. A dual polymer/liquid electrolyte of [SPE //Glass fiber//[0.4 M Mg_2Cl_3+·$AlPh_2Cl_2$-/THF (APC) liquid electrolyte]] is engineered and its structural, electrical and electrochemical properties investigated. Prototype Mg-cells have been constructed using BTO cathode and Mg-metal anodes. Furthermore, the performance before and after heating and with/without pre-magnesization of the BTO electrode have been carried out. The results indicate that the introduction of a dual electrolyte and heated magnesized BTO cathode material could be an effective approach to engineering the performance of the rechargeable and quasi-solid-state Mg batteries.

Experimental

Electrolyte synthesis

All chemicals used were purchased from Alfa Aesar except graphene nanoplatelets (GNPs, Grade M, XG Science). PVdF-based polymer electrolyte was prepared by dissolving 3 g of PVdF in 20 ml of methyl-2-pyrrolidinone (NMP), and 1.5 ml of tetraethelene glycol dimethyl ether (TEGDME), with 2 g magnesium trifluoromethanesulfonate powder ($Mg(O_3SCF_3)_2$). This

mixture was stirred for 24 hours and then dried at 55 °C in a vacuum oven, Fig. S1. Liquid electrolyte 0.4 M $Mg_2Cl_3^+ \cdot AlPh_2Cl_2^-$/THF (APC) was prepared according to Ref. [16].

BTO/GNP synthesis

BTO/GNP composite was synthesized by grinding 0.9 g BTO and 0.1 g GNP for 20 minutes, then the 10 ml acetonitrile was added and stirred for 24 hrs. Finally, the solution was heated at 200 °C for 120 minutes and quenched at to ~ -5 °C.

Materials characterization

Thermogravimetric analysis (TGA) of all materials was performed on an SDT-Q600 (USA) instrument under an oxygen flow at a heating rate of 10 ˚C min^{-1}. Fourier transform infrared spectroscopy (FTIR) was collected with a Perkin Elmer spectrophotometer. UV−vis spectra were carried out in absorption mode on a JENWAY 6405 UV−vis spectrometer. XRD data for the $BaTiO_3$ and $BaTiO_3$/GNP series (deposited on aluminum foils) was carried out on a Smart-Lab X-ray diffractometer (XRD, Rigaku Corporation, Japan) equipped with line focus Cu-Kα radiation (λ ~ 1.5406 Å, a step scan of 0.02º and 3 s per step). Rietveld refinements with structural models using X-ray diffraction data were carried out using GSAS II [17]. Field emission scanning electron microscopy (FE-SEM, Merlin Compact, Zeiss, Germany) equipped with energy dispersive spectroscopy (EDS, X-MaxN, Oxford, UK) was used to reveal the microstructure and chemical composition.

Electrochemical measurements

The ionic conductivities of the electrolytes were measured by electrochemical impedance spectroscopy (EIS) with alternating current (AC) amplitude of 5 mV in the frequency range of 10^5–0.1 Hz at temperatures from 25 to 90 °C on a Solartron electrochemical station 1260+1287.

The electrolyte was sandwiched between two stainless-steel blocking electrodes to form the test cells; the cells were kept at each test temperature for 30 min to reach thermal equilibrium.

0.1 mm thick Mg foils were used to carry out the electrochemical performance; the surfaces of the foils were polished to remove the insulating surface oxide layer. The electrochemical stabilities of the samples were examined using linear sweep voltammetry (LSV) of Mg//electrolytes//SS cells at a scanning rate of 80 mV s^{-1} from -1.0 to 4.0V at 55˚C. Galvanostatic cycling curves of the symmetric Mg | electrolyte | Mg cell were measured on a NEWARE BTS4000 testing system at 55˚C. The interface stabilities of the electrolytes against a Mg-metal electrode were examined by recording the values of impedance of Mg//SPE//Mg, Mg//APC//Mg and Mg//[APC/fiber glass separator/SPE]//Mg symmetric cells for different storage times at temperature = 55 ˚C and the frequency = 1000 Hz. The magnesium ion transference number of electrolytes at 55 °C was measured by AC impedance and direct-current (DC) polarization (with a DC voltage of 150 mV) using a symmetric Mg//electrolyte//Mg cell.

The working electrodes were prepared with as-prepared BTO or BTO/GNP composite powders, Super P carbon black, and polyvinylidene fluoride (PVdF) binder at a weight ratio of 8:1:1 and the resulting slurry was coated on copper foil after uniform grinding in NMP solvent and then dried under vacuum at 120 ˚C for 2 h. CR2032-type coin cells were assembled in an Ar-filled glove box. The average loading of BTO electrode was about 0.9 mg cm^{-2}. The coin cells were charged with constant capacity or galvanostatically to 2 V depending on what was reached first and discharged to 0.1 V vs. Mg^{2+}/Mg. Glass fiber was used as a separator. A galvanostatic cycle test was carried out by a commercial battery testing system (NEWARE BTS4000) at 55 ˚C. Magnesiation of BTO and BTO/GNP were performed by initially discharging Mg/Electrolyte/BTO and Mg/Electrolyte/[BTO/GNP] coin cells, then extracting and heating

beyond the ferroelectric transition at 150 ˚C for use in fresh cells. Electrochemical impedance spectroscopy (EIS), cyclic voltammetry (CV), linear seep voltammetry (LSV) and time evolution were conducted by CHI604 electrochemical workstation. The collected impedance data was analyzed by ZView software.

Results and Discussions

The solid polymer electrolyte (SPE) were prepared by casting the mixture of PVdF, NMP, TEGDME and $Mg(CF_3SO_3)_2$. Fig. 1 (a-c) show SEM images of PVdF, PVdF/TEGDME and (PVdF/TEGDME)/$Mg(CF_3SO_3)_2$ polymer composites films (SPE), respectively. The pristine PVdF film shows microsphere morphology with size of a several micrometers and small pores. After introducing TEGDME onto the polymer matrix, the radius of the microspheres is reduced to ~ 5 % of the pristine, which is attributed to the TEGDME acting as scissors for the polymer chains. It is worth mentioning that the addition of salt to the polymer has presented a completely different morphological structure. Note, the C=O polar group of TEGDME can assist in the dissociation of $Mg(CF_3SO_3)_2$. The number of the pores was also found to increase after the addition of the salt, which can further potentially facilitate the diffusion of Mg^{2+}.

XRD patterns of pristine PVDF, PVDF/NMP dried, (PVDF/NMP)/TEGDME, and SPE are shown in Fig.1(d). It can be seen that the peak at $2\theta = \sim 20°$ is still discernible for the samples. The XRD pattern of PVDF can be indexed to that of α-phase PVDF[18], with the introduction of TEGDME and $Mg(CF_3SO_3)_2$ salt, the diffraction profiles of the films became broader, which suggest a decrease in crystallinity.

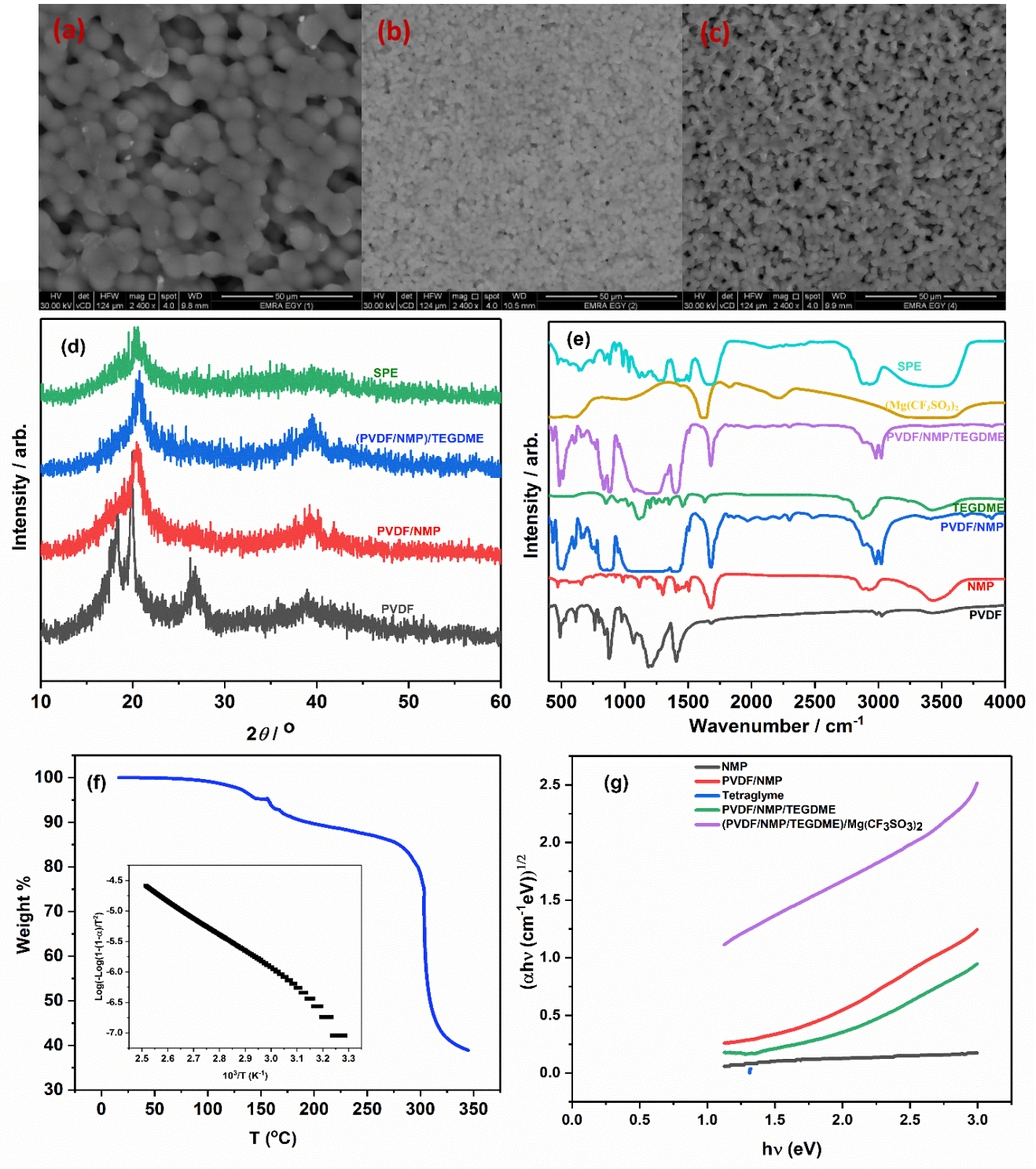

Fig.1 SEM micrographs of (a) PVDF (b) PVDF/TEGDM (c) SPE; (d)XRD of PVDF, PVDF/NMP, (PVDF/NMP)/TEGDME and SPE films; (e) FTIR spectra of solvents and SPE at different synthesis stages; (f)TGA diagrams of SPE; (g) Direct energy band gap graph for solvents and SPE at different synthesis stages.

Fig. 1(e) displays the Fourier transform infrared spectroscopy (FTIR) of PVDF, NMP, PVDF/NMP, TEGDME, (PVDF/NMP)/TEGDME and SPE. The bands located at 3043, 2998, 1411, 765 and 489 cm^{-1} were assigned to CH_2 symmetric stretching, CH_2 asymmetric stretching, CH_2 in plane bending, CF_2 in plane bending or rocking and CF_2 bending and wagging of the crystalline pristine PVDF[19], respectively. With the introduction of TEGDME and $Mg(CF_3SO_3)_2$ salt, all the characteristic bands of PVDF and NMP broaden and shift after reaction of TEGDME and $Mg(CF_3SO_3)_2$ with PVDF. Generally, the characteristic absorption peaks of PVDF, NMP, TEGDME, and $Mg(CF_3SO_3)_2$ disappear or change as a result of the different chemical environments in the SPE.

The thermal stability is an important indicator of whether a battery can operate safely at high temperature. Fig. 1(f) shows the TGA curve of SPE, which consists two steps of weight loss, the decomposing activation energy $E_a = 2.303\ slope \times R$ in the temperature range 16-120 ^oC was calculated using the Coats-Redfern equation[20] $[log\frac{-\log(1-\propto)}{T^2}] = \log\left[\frac{(1-2RT/E)AR}{\beta E}\right] - \frac{E}{2.303RT}$, where R is universal gas constant, the slope is obtained from the relation between $\log[-\log(1-\propto)/T^2]$ and $1000/T$ (inset Fig. 1(f)), $\propto = \frac{w_i - w_t}{w_i - w_f}$, w_i, w_t and w_f are the initial weight, the weight at given temperature, sample weight at the end of reaction, respectively. The activation energy E_a was calculated ~ 57.6 kJ mol^{-1} ~ 23.2 kT N_A(N_A is Avogadro number). This relatively high value suggests a larger amount of heat is required to perturb the system and indicates good thermal stability of SPE below 100 ^oC. The high decomposing activation energy of SPE is essential to the safety of the quasi solid state battery. Furthermore, SPE retains 99 wt.% of its initial weight below 100 ^oC. The minor weight loss at ~100 ^oC is most possibly due to the presence of trapped moisture and volatile solvents[21]. Differentiating the TGA curve exhibits

sharp peak at 158 °C and 306 °C corresponding to the SPE melting and decomposition points, respectively. It should be noted that the SPE melting point (158 °C) is lower than the PVdF melting point (177 °C). Significant weight loss occurs in the range of 150°C ~ 320°C due to the degradation of C-F unit and decomposition of SPE[22].

UV–Visible absorption spectroscopy data was used to study the impact of solvent and salt on the physical properties of PVDF. The optical energy band gap is derived from Tauc's plot $\alpha h\nu = K[h\upsilon - E_g]^n$, $\alpha = 2.303\frac{\mathrm{A}}{t}$ is the absorption coefficient, h is the Planck's constant, K is the constant depending on structure of specimen, υ is the incident light frequency, E_g is the energy band gap, $n = \frac{1}{2} or\ 2$ for allowed direct or indirect transition, A is the absorbance and t is the thickness of sample. Fig. 1(g) shows the variation of $(\alpha h\nu)^{\frac{1}{2}}$ vs $h\upsilon$ for NMP, PVDF/NMP, TEGDME, PVDF/NMP/TEGDME, and SPE. E_g values were calculated from extrapolation [23]. The E_g values of pure PVDF drop from 5.2 eV[24] to 1.96 eV after dissolving in NMP and TEGDME and to 1.46 eV after adding $Mg(CF_3SO_3)_2$ salt. This further indicates that the solvent and salt perturb the bonding scheme (change in bond angles and/or bond lengths) inducing structural modifications in the PVDF matrix to produce the localized states in the optical band gap, which are clearly reflected in the E_g values. This physical nature change may be the reason behind Mg^{2+} mobility improvement (discussed below).

Fig. 2(a) exhibits the temperature dependence of ionic conductivities of APC, SPE and APC/SPE electrolytes from 25 to 90 °C. APC displays remarkably high conductivity of 2.59×10^{-3} S cm^{-1} at room temperature. A slight decrease in ionic conductivity was observed when increasing the temperature beyond 60 °C, mainly because the partial evaporation of THF. For

SPE, the conductivity increases nearly linearly to 60 °C and then changes slightly. Two regions were fit to the Arrhenius equation:-

$$\sigma = \sigma_o exp^{\frac{-E_a}{KT}}$$

where σ_o represents the pre-exponential factor of conductivity, E_a is the activation energy for ion conduction, and K is Boltzmann constant. It is noted that E_a for the first region (25-60°C) is 0.62 eV and decreases to 0.19 eV for the second region (60-90°C). This suggests that the ions require lower energy for migration in the second region. Compared with SPE electrolyte, significant improvement in ionic conductivity is observed using APC/SPE electrolyte. The disappearance of the curvature and change in slope at 60 °C could be related to the change in the structure of the electrolyte. In addition, fitting E_a for APC/SPE is results in a low value (0.07 eV), a sign of a low energy barrier for Mg^{2+} transfer in the APC/SPE electrolyte.

LSV measurements were used to evaluate the effect of a liquid electrolyte on the electrochemical oxidative stability of the SPE. LSV measurement was performed on a coin cell (using stainless steel (SS) as the working electrode and Mg foil as the counter and reference electrode) to investigate the electrochemical stability of all electrolytes. Fig. 2b presents the LSV curves to test the electrochemical-stability window of three electrolytes including APC, SPE, and APC/SPE at 55 °C. A mild current peak is observed at ~1.0 V for the SPE electrolyte while no peaks or apparent anodic current are observed from 0.5 to 2.5 V for the APC/SPE electrolyte. The results clearly show that integration of the liquid electrolyte with SPE dramatically increases the oxidative stability up to 2.5 V that could match well with high-voltage cathode for high energy-density batteries. To evaluate the interfacial performance, the reversibility of Mg plating

and stripping processes in APC, SPE, and APC/SPE electrolytes were investigated in symmetric Mg/Mg cells. All the symmetric Mg/Mg batteries were charged and discharged at a current density of 0.02 mA cm^{-2}. As shown in Fig. 2c, compared with SPE and APC, for the initial cycles, the stripping and plating of Mg metal in APC/SPE occurs at a relatively low overpotential. However, after that, the gradual increase in the peak-to-peak voltage is indicative of the higher barrier of the plating / stripping Mg segments of the cycle, presumably because the gradual growth of the interfacial resistance that end the cycle life after 2000 min. Generally, integrating APC with SPE can effectively reduce polarization phenomenon, thereby improving the electrochemical performance of the SPE.

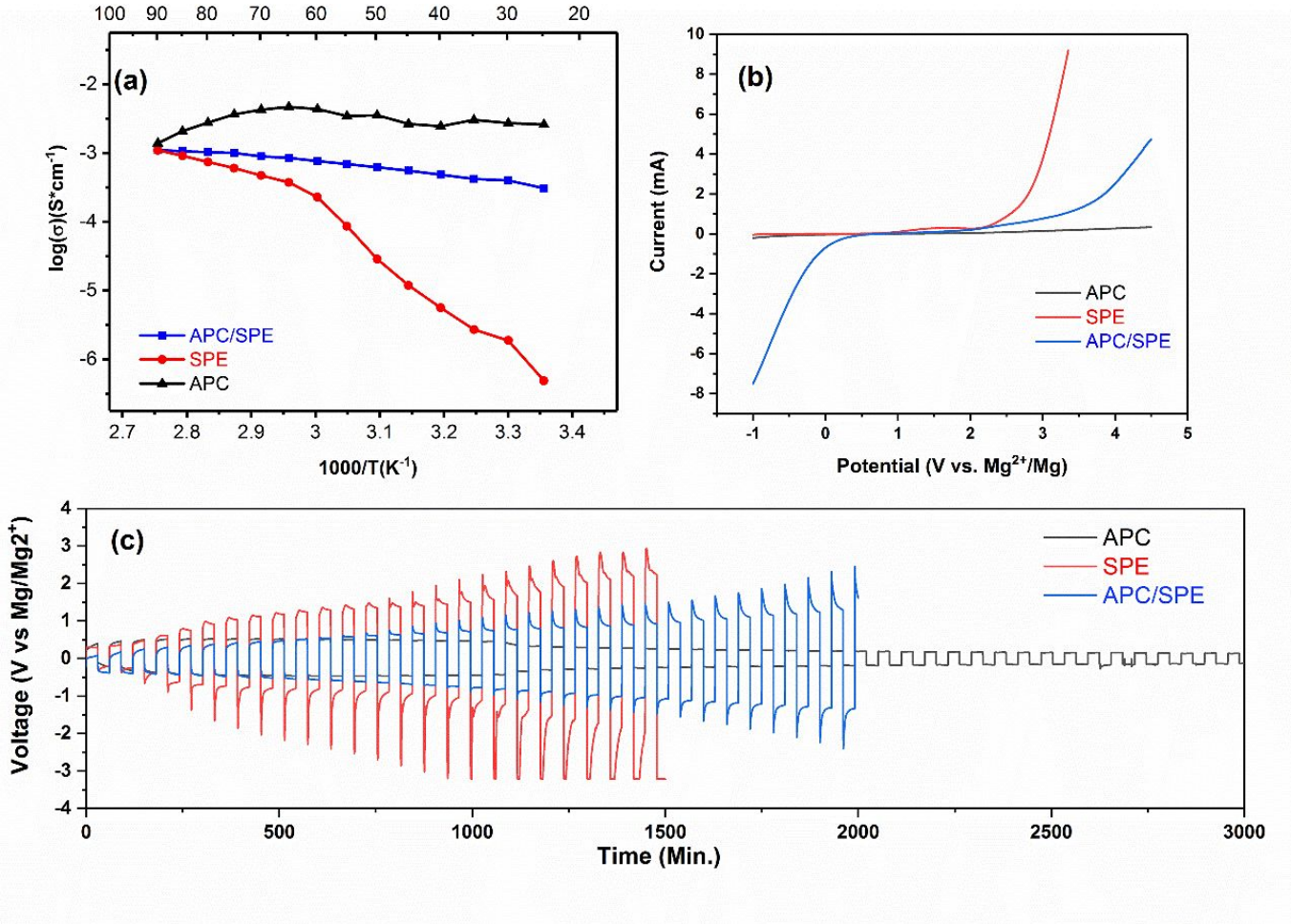

Fig.2 (a) temperature dependent of ionic conductivity for APC, SPE and APC/SPE electrolytes; (b) LSV curves of Mg//electrolytes//SS coin cells; (c) Mg stripping/plating curves of a Mg // electrolyte // Mg cell at 0.02 mA cm^{-2}, at 55 °C.

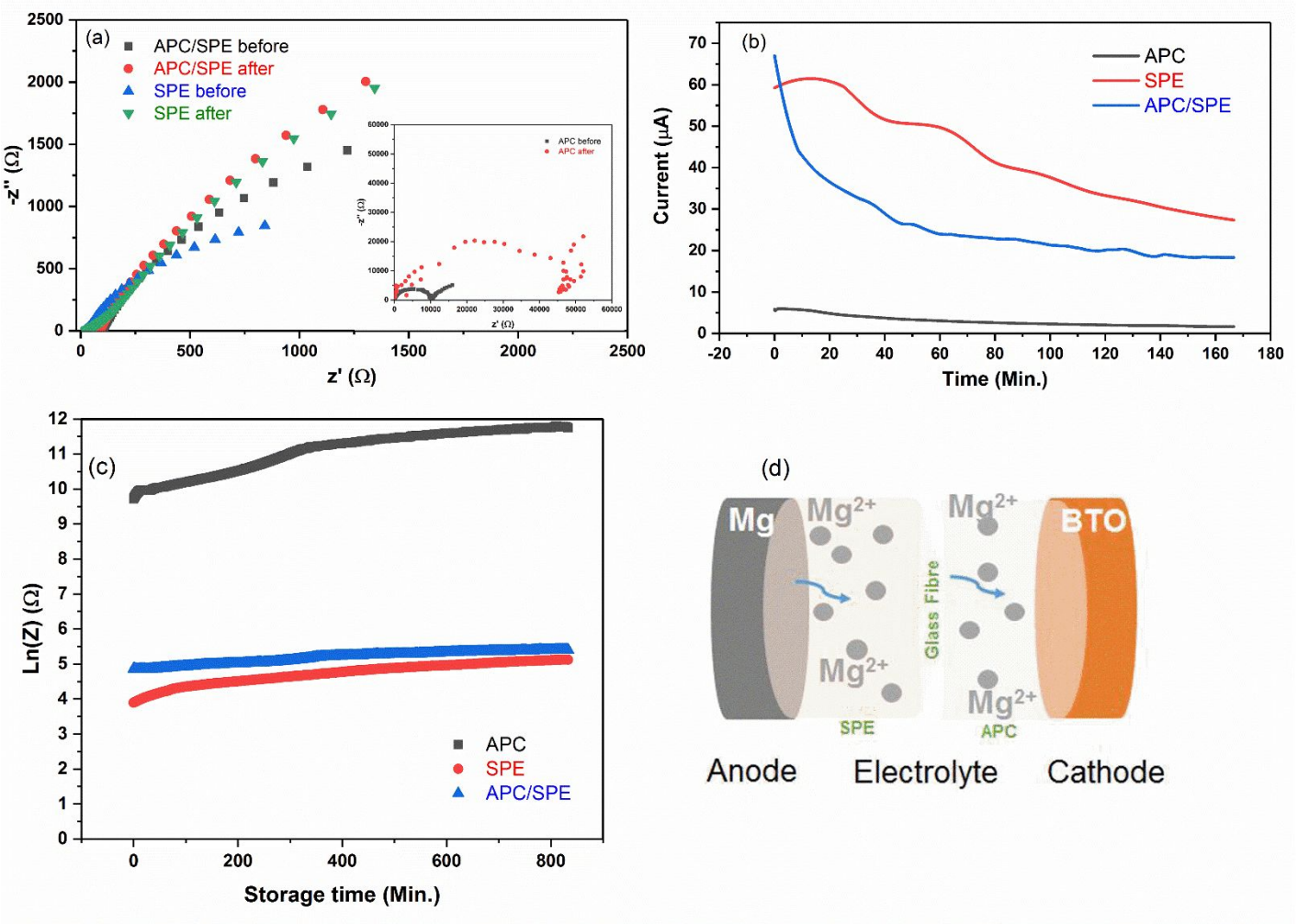

Fig.3 At 55 °C (a) Nyquist plots of a Mg//electrolytes//Mg cell before and after DC polarization; (b) DC polarization curve of the symmetrical of Mg//electrolytes//Mg; (c) time evolution of the interfacial resistances of Mg//electrolytes//Mg symmetric cells; (d) schematic illustration of Mg//APC/SPE//BTO battery.

From the variation of AC impedance spectra before and after polarization and the polarization current with time as shown in Fig. 3 (a) and (b), the Mg^{2+} transference numbers $t_{Mg^{2+}}$ of APC, SPE and APC/SPE were measured. The Evans–Vincent–Bruce equation[25] were used to calculate the fraction of Mg^{2+} migration of various ionic species in APC, SPE and APC/SPE electrolytes:

$$t_{Mg^{2+}} = \left[\frac{I_s(\Delta V - R_0 I_0)}{I_0(\Delta V - R_s I_s)}\right] \quad (1)$$

where I_0 and I_s refer to the initial and steady state current, respectively, R_0 and R_s are the initial and steady state charge transfer resistances, respectively. The $t_{Mg^{2+}}$ = 0.74 of APC/SPE at 55 °C is higher than that of APC ($t_{Mg^{2+}}$=0.21) and SPE ($t_{Mg^{2+}}$=0.41). The higher $t_{Mg^{2+}}$ of APC/SPE indicates that the ion conduction in APC/SPE dual electrolyte is mainly accomplished by the Mg^{2+} [26]. This result confirms that the introduction of the dual electrolyte systems can play a role as a two-layer filter that prevents the passage of undesirable molecules and ions, only allows magnesium ions to pass at relatively good rates. A high $t_{Mg^{2+}}$ = 0.74 of APC/SPE at 55 °C may be an important factor to reduce the growth of Mg^{2+} dendrite, decrease safety issues, suppress passive reactions on the electrodes and decrease over-potential[27-28].

The stability of the electrode–electrolyte interface is a critical factor to influence the cycling performance of batteries. Fig. 3(c) depicts the time evolution of the AC impedance spectra of the Mg/Mg symmetrical cell of three electrolytes including APC, SPE, and APC/SPE at 55 °C. As shown, the internal resistance of the cell with APC electrolyte increases continuously with time due to the reaction between APC and Mg metal suggesting the growth of a stable Mg-containing semi-conductive passivation layer on the surface of the Mg metal electrode. In contrast, the total impendence of cell with APC/SPE has a small change after 10 h, which indicates that APC/SPE

has the ability to reduce undesirable chemical reaction at the interface with Mg metal compared with APC and SPE.

Fig. 3(d) shows schematic illustration of Mg//[APC/fiber glass separator/SPE]//BTO battery. In this work, two kinds of the electrodes (BTO and BTO/GNP) were used to assemble the coin cells. BTO and BTO/GNP were also extracted from a discharged Mg cell (magnesized) and heated to 150 ˚C and then were placed into fresh batteries and run. EIS was performed on all electrode materials to calculate the diffusion coefficient. Fig. 4(a) shows the Nyquist plots of BTO and BTO/GNP electrodes before and after magnesiation/heating in APC electrolyte. All Nyquist profiles exhibit semicircles that are separated from the origin by ohmic contact resistance R_s of the electrolyte and electrode in a high frequency range and two semi-circles observed at high and medium frequencies. The diameter of the semicircle at high and medium frequencies represents the bulk resistance and electrolyte/electrode's charge transfer resistance (R_{ct}), respectively. The inclined line represents Mg^{2+} ion diffusion resistance in the BTO electrode known Warburg impedance Z_w. The fitted kinetic parameters are displayed in Table S1. The diffusion coefficient of magnesium at the electrode-electrolyte interface $(D_{Mg^{2+}})$ could be calculated as:

$$D_{Mg^{2+}} = \left[\frac{R^2T^2}{2A^2n^4F^4C^2\sigma^2}\right] \qquad (2)$$

R=8.314 J / mol. K and T= 328 K were gas constants and absolute temperature, respectively. A is the cathode area in touch with the electrolyte (1.5 cm^2), n is the number of electrons involved, F is the Faraday constant 96485 C mol^{-1}, C is the concentration of magnesium ions mol. cm^3 and σ is the Warburg factor, which is related to Z' via:- $Z_{Re} = R_s + R_{ct} + \sigma\omega^{-\frac{1}{2}}$ and σ is obtained by the slope of the lines in Fig. 4(b) (at low frequencies). The diffusion coefficients $D_{Mg^{2+}}$ of

magnesium ions in BTO electrodes are calculated by Eq.2 and are listed in Table S1. As shown, the low values of $D_{Mg^{2+}}$ confirm that the Mg-ion diffusion energy barrier in all electrodes is high. The $D_{Mg^{2+}}$ values in pre-magnesiation and thermal treated BTO cathodes are much higher than that in pristine BTO, implying better kinetics in the treated electrodes

Magnesium reactivity in BTO electrodes was investigated by conducting CV measurement in a potential range of 0-2.2 V vs. Mg/Mg^{2+} with a scan rate 80 mV s^{-1} as shown in Fig. 4 c and Fig S2. Although there is a clear oxidation peak located around 0.7 V and the reduction peak is located around 1.8 V resulting from the Mg^{2+} interaction with BTO, the general behavior can be linked to more electrochemical capacitive storage processes[29]. Fig. 4(d) and Fig. S2 present the initial galvanostatic discharge/charge curves of fresh and discharged/heated BTO, BTO/GNP electrodes at current density of 20 mA g^{-1}. APC, SPE and APC/SPE were used as electrolytes for comparison. In Fig. 4 (d), it can be seen that the heated/magnesized BTO electrode delivers a high specific capacity of 507 mAh g^{-1}, which is higher than that for heated/magnesized BTO/GNP (219 mAh g^{-1}), BTO (436 mAh g^{-1}), and BTO/GNP (371 mAh g^{-1}), in APC electrolyte, respectively. For SPE, the BTO and heated/magnesized BTO possess high specific capacity of 788 and 691 mAh g^{-1} respectively, compared to 437 and 456 mAh g^{-1} for non-treated BTO/GNP, and heated/magnesized BTO/GNP, respectively. For APC/SPE, the BTO, heated/magnesized BTO and heated/magnesized BTO/GNP electrodes possess high specific capacity of 530, 557 and 632 mAh g^{-1}, respectively, compared to 149 mAh g^{-1} for BTO/GNP. For APC, SPE and APC/SPE, heated/magnesized BTO shows high discharge voltage plateaus around 0.9 V compared non-treated BTO. The pre-magnesiation and thermal treatment of BTO appears to have an impact on the electrochemical properties. It is interesting to note the variability in performance based on the different electrode/electrolyte combinations which in part

shows that the combination of these need to be considered for Mg-based battery technologies. The experimental setup of the charge capacity could be fixed at 75 mAh g^{-1} or a cutoff voltage of 2 V to avoid electrolyte reduction. For SPE, reaching the cutoff voltage = 2 V typically occurs rapidly, while there is evidence for electrolyte reduction in APC electrolyte. Introduction of APC/SPE electrolyte results a more stable behavior compared APC and SPE specially in case of pre-magnesized and thermally treated BTO, for example Mg//[APC/SPE]//BTO shows very stable cycling at ~ 68 mAh g^{-1} for more than 15 cycles, Fig. 4(e) and 4(f), whereas the Mg//APC//BTO and Mg//SPE//BTO cells decay dramatically within initial cycles, Fig.4 (f). This may be attributed to the potential of the lowest unoccupied molecular orbital (LUMO) is higher than the Fermi level of anode for APC/SPE electrolyte; while the potential of the highest occupied molecular orbital (HOMO) is lower than the potential of Fermi level of the cathode. Inset Fig. 4(e) shows three series connected Mg//dual electrolyte//BTO coin cells which can successfully light up a red light-emitting diode (LED) for more than 15 mins. Fig. 5(a-e) shows the scanning electron microscopy (SEM) images of pristine, magnesized and heated/magnesized BTO and BTO/GNP cathode using APC and APC/SPE electrolytes. It can be seen in Fig 5(a-f) that the pristine BTO cathode surface shows a typical morphology of irregular micro-grains of a few micrometers and small pore distribution. After discharging to 0.01 V, the BTO cathode surface displays small cracks and lower porosity, indicating a surface-level change. The surface of the heated/magnesized BTO becomes smooth but cracks still appear. Similarly, the BTO/GNP surface also depicts a typical morphology of irregular micro-grains of a few micrometers with what appears to be large-size flakes of GNP nanosheets. However, no cracks were observed after magnesization/heating. Moreover, EDS mapping analysis was carried out for all the samples to observe Mg element distribution. As shown in Fig.5 (g-m), EDS data suggests that the ratio of Mg

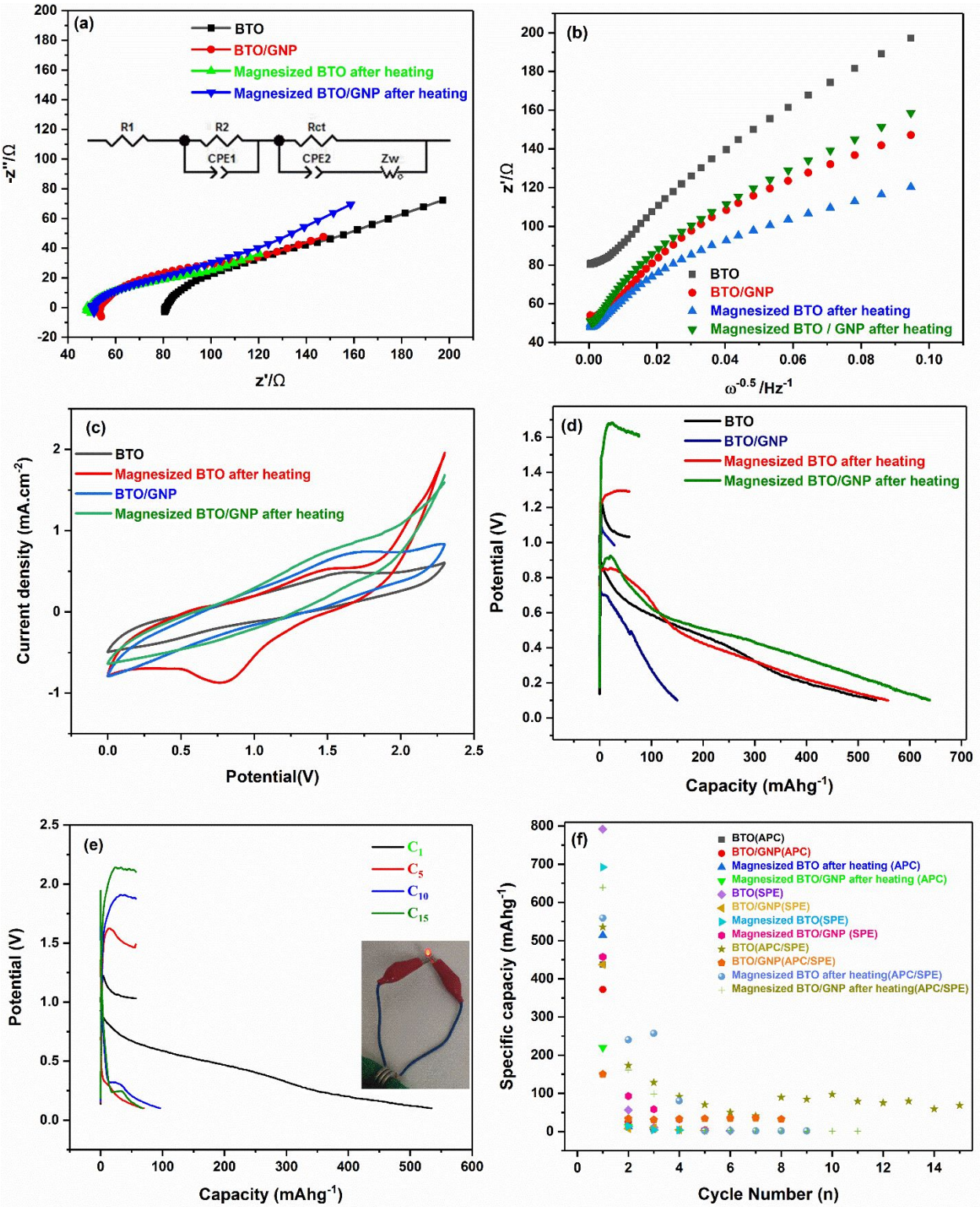

Fig. 4 At 55 °C (a) electrochemical impedance spectra (EIS); (b) linear fitting of Warburg impedance; (c) Cyclic voltammetry (APC)(d) Discharge/charge profile (APC/SPE); (e) discharge/charge profile Mg//[APC/SPE]//BTO at different cycles with inset cell light up a LED; (f) specific capacity versus cycle number.

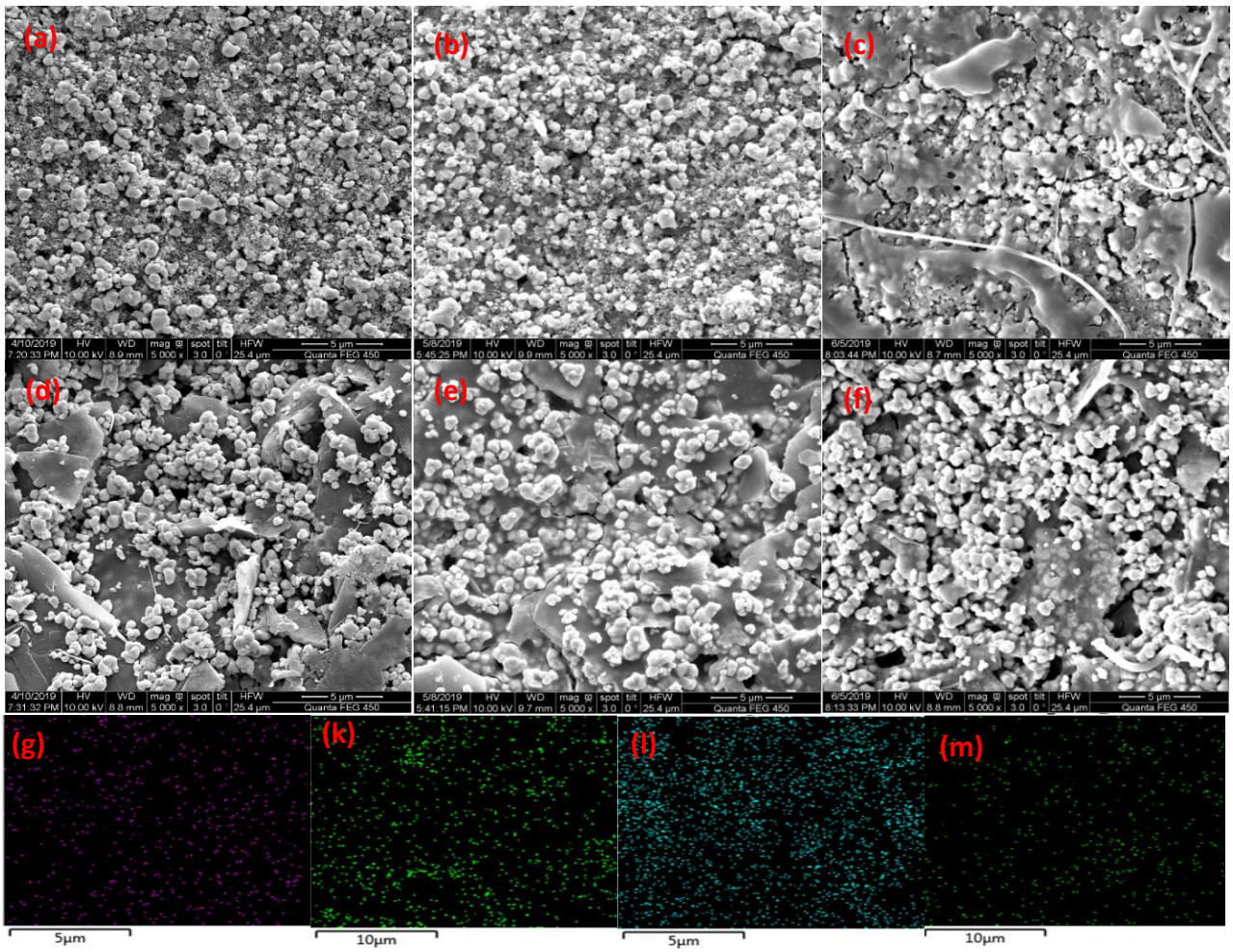

Fig. 5 SEM micrographs of BTO at (a) pristine; (b) after discharge; (c) magnesized/heated and discharged; BTO/GNP at (d) pristine, (e) after discharge, (f). magnesized/heated and discharged using APC/SPE electrolyte and Mg anode; EDS mapping images of BTO cathode, (g) after discharge (Mg= 0.4%) (k), magnesized/heated and discharged (Mg=4.9%). BTO/GNP cathode (i) after discharge (Mg= 3.7%), (m) magnesized/heated and discharge (Mg=1.6%).

atoms is consistent with the discharge time, Mg wt.% increased from 0 for pristine to 0.4 and 4.9 for discharged and heated/magnesized/discharged BTO, respectively. The comparison X-ray diffraction (XRD) patterns collected at room temperature of BTO and BTO/GNP (deposited on aluminum foils) using APC electrolyte, magnesiation and magnesiation/heated series are shown in Fig. 6 (a,b). All samples adopt tetragonal *P*4*mm* symmetry for $BaTiO_3$ with minimal changes[30].

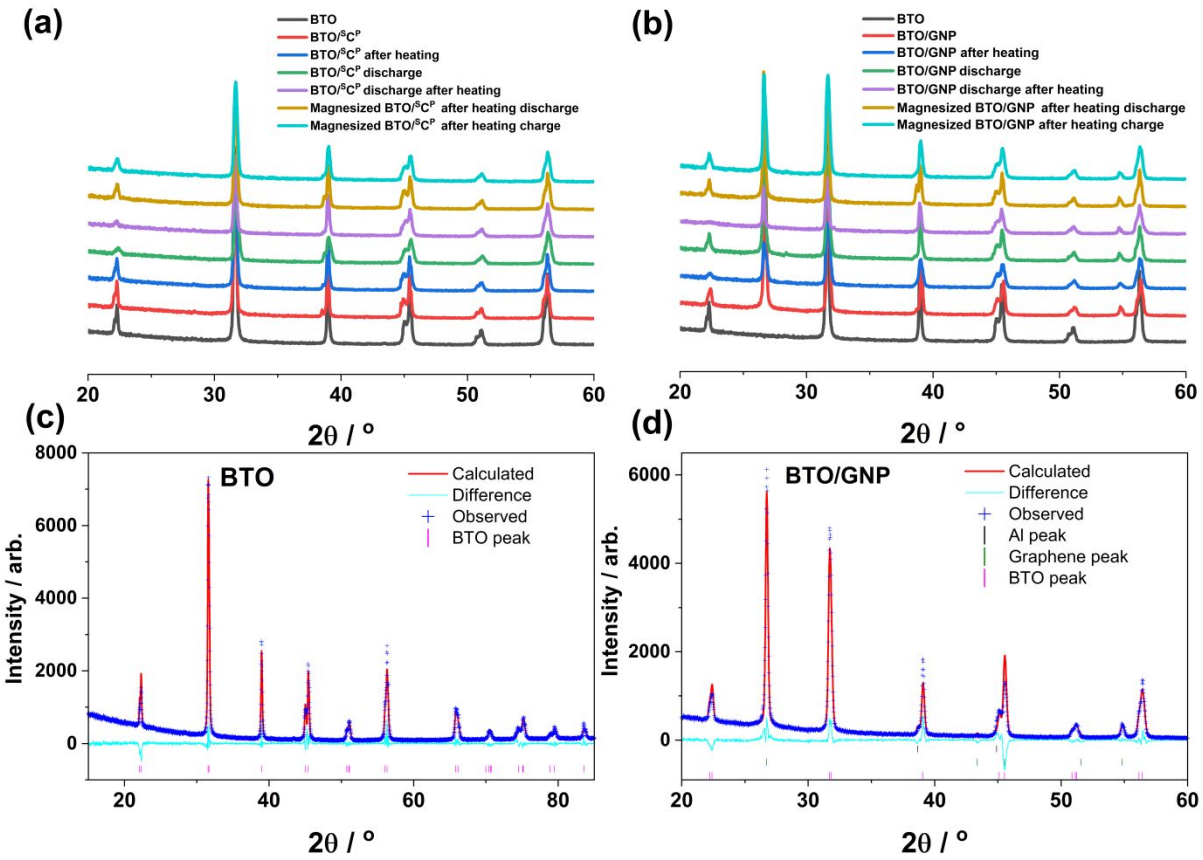

Fig. 6 Comparison of XRD patterns for different conditions of (a) BTO, (b) BTO/GNP; and Rietveld-refined fits of (c) pristine BTO, and (d) BTO/GNP

This indicates that the Mg interaction doesn't change the long-range ordered $BaTiO_3$ crystal structure and the structure doesn't change with magnesization or thermal treatments when measured at room temperature. Minute intensity fluctuations were noted for some discharged samples. Rietveld analysis results are presented in Fig. 6 (c-d) and Fig. (S3, S4), the corresponding lattice parameters can be found in Table 1 and Table S2, and the crystal structure in Fig. 7. Combining with the electrochemical performance and XRD results, we can conclude that the electrochemical reactions mainly happen at the surface or near surface (Mg ion adsorption/desorption process)[29]. It is clear also that the effect of magnetisation/heating at BTO was only on the surface in generating more active sites can adsorb/desorb Mg^{2+}.

Table.1 Refined crystallographic parameters for BTO and BTO/GNP and magnesized/heated versions. The remaining data provided in the supporting table S2.

Sample	Rwp	*a*	*b*	*C*	Volume	Atom	x	y	Z
BTO	7.79%	3.9946(1)	3.9946(1)	4.0299(2)	64.31(1)	Ba1	0	0	0.0035(20)
						Ti1	0,5	0,5	0.507(10)
						O1	0,5	0,5	-0.0547(31)
						O2	0,5	0	0.49(3)
BTO/GNP	12,76%	3.9951(10)	3.9951(10)	4.0299(9)	64.32(5)	Ba1	0	0	0.023(4)
						Ti1	0,5	0,5	0.510(28)
						O1	0,5	0,5	-0.043(31)
						O2	0,5	0	0.51(14)

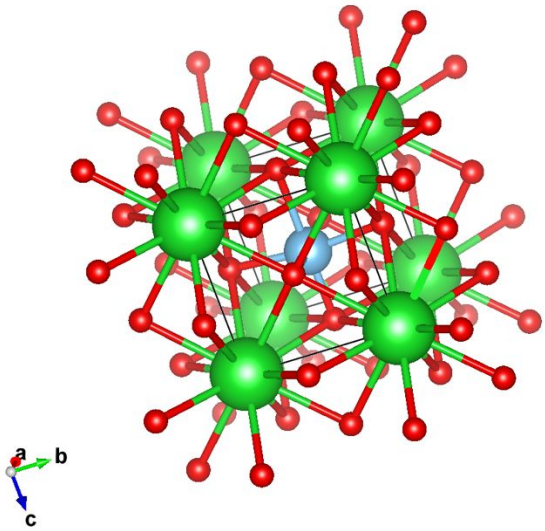

Fig. 7 The representation of unit cell of tetragonal BTO (light blue= Ti, Green= Ba, Red= O) with a=3.9946(1), c=4.0299(2).

Conclusions

In summary, we present a new approach to modify the interfaces between electrodes and the electrolyte in the Mg batteries. A polymer electrolyte consisting of PVDF, TEGDME and $Mg(O_3SCF_3)_2$ has been fabricated and characterized. This dual polymer shows notable good behavior for quasi-solid-state Mg batteries. Dual electrolyte exhibits a remarkable Mg-ion conductivity up to 4.62×10^{-4} S cm^{-1} at 55 ºC, a high transfer number ($t_{Mg^{2+}}$ = 0.74), low over potential and stable Mg stripping and plating in the initial cycles. Moreover, BTO shows a very stable structure that does not change with magnesiation (or heating and magnesiation at room temperature). Furthermore, the cell based on the dual electrolyte and pre-magnesiation and thermally treated BTO cathodes delivered a high initial discharge capacity and stable cycling around 68 mAh g^{-1} for more than 15 cycles. The Mg^{2+} ions existence on the surface of BTO after discharge was

confirmed by EDS. Our work presents a strategy to develop electrolyte and design new cathode for further exploration which may provide a springboard to many more future studies.

Supporting Information

Table **S1**. Electrochemical impedance parameters of BTO electrodes. Table **S2**. Structural parameters for BTO before and after magnesiatiation/heating. **S1.** Photograph of a PVDF-based polymer electrolyte. **S2.** Cyclic voltammetry and discharge/charge profile of BTO electrodes using SPE, APC/SPE electrolytes. **S3.** Rietveld fitted graphs of BTO electrodes before and after magnesiation and heating. **S4.** Rietveld fitted graphs of BTO/GNP electrodes before and after magnesiation and heating.

AUTHOR INFORMATION

Corresponding Author:

*E-mail: islam.shihah@fsc.bu.edu.eg

Acknowledgements

This work is financially supported by National Basic Research Program of China (2017YFE0113500) & Science Technology Development Fund, Chinese-Egyptian Research Fund (CERF) (Grant No. 30340). J.L. would like to thank the support of the China Scholarship Council and UNSW for Ph.D. funding.

References

(1) Tröger-Müller, S.; Liedel, C. A Zwitterionic Liquid Electrolyte for Magnesium Batteries. *Batteries & Supercaps* **2019,** *2* (3), 223-228.
(2) Sheha, E.; El-Deftar, M. Magnesium hexakis (methanol)-dinitrate complex electrolyte for use in rechargeable magnesium batteries. *Journal of Solid State Electrochemistry* **2018,** *22* (9), 2671-2679.

(3) Luo, L.; Zhen, Y.; Lu, Y.; Zhou, K.; Huang, J.; Huang, Z.; Mathur, S.; Hong, Z. Structural evolution from layered Na 2 Ti 3 O 7 to Na 2 Ti 6 O 13 nanowires enabling a highly reversible anode for Mg-ion batteries. *Nanoscale* **2020,** *12* (1), 230-238.
(4) Attias, R.; Salama, M.; Hirsch, B.; Goffer, Y.; Aurbach, D. Anode-electrolyte interfaces in secondary magnesium batteries. *Joule* **2018**.
(5) Wang, Y.; Xue, X.; Liu, P.; Wang, C.; Yi, X.; Hu, Y.; Ma, L.; Zhu, G.; Chen, R.; Chen, T. Atomic Substitution Enabled Synthesis of Vacancy-Rich Two-Dimensional Black TiO2–x Nanoflakes for High-Performance Rechargeable Magnesium Batteries. *ACS nano* **2018,** *12* (12), 12492-12502.
(6) Mohtadi, R.; Matsui, M.; Arthur, T. S.; Hwang, S. J. Magnesium borohydride: from hydrogen storage to magnesium battery. *Angewandte Chemie International Edition* **2012,** *51* (39), 9780-9783.
(7) Aurbach, D.; Lu, Z.; Schechter, A.; Gofer, Y.; Gizbar, H.; Turgeman, R.; Cohen, Y.; Moshkovich, M.; Levi, E. Prototype systems for rechargeable magnesium batteries. *Nature* **2000,** *407* (6805), 724.
(8) Chu, I.-H.; Zhang, M.; Ong, S. P.; Meng, Y. S. Battery Electrodes, Electrolytes, and Their Interfaces. *Handbook of Materials Modeling: Applications: Current and Emerging Materials* **2018**, 1-24.
(9) Liu, C.; Neale, Z. G.; Cao, G. Understanding electrochemical potentials of cathode materials in rechargeable batteries. *Materials Today* **2016,** *19* (2), 109-123.
(10) Shao, Y.; Rajput, N. N.; Hu, J.; Hu, M.; Liu, T.; Wei, Z.; Gu, M.; Deng, X.; Xu, S.; Han, K. S. Nanocomposite polymer electrolyte for rechargeable magnesium batteries. *Nano Energy* **2015,** *12*, 750-759.
(11) Osman, Z.; Zainol, N.; Samin, S.; Chong, W.; Isa, K. M.; Othman, L.; Supa'At, I.; Sonsudin, F. Electrochemical impedance spectroscopy studies of magnesium-based polymethylmethacrylate gel polymer electroytes. *Electrochimica acta* **2014,** *131*, 148-153.
(12) Kumar, G. G.; Munichandraiah, N. Solid-state rechargeable magnesium cell with poly (vinylidenefluoride)–magnesium triflate gel polymer electrolyte. *Journal of power sources* **2001,** *102* (1-2), 46-54.
(13) Pandey, G.; Agrawal, R.; Hashmi, S. Magnesium ion-conducting gel polymer electrolytes dispersed with nanosized magnesium oxide. *Journal of power sources* **2009,** *190* (2), 563-572.
(14) Megaw, H. D. Temperature changes in the crystal structure of barium titanium oxide. *Proceedings of the Royal Society of London. Series A. Mathematical and Physical Sciences* **1947,** *189* (1017), 261-283.
(15) Jiang, B.; Iocozzia, J.; Zhao, L.; Zhang, H.; Harn, Y.-W.; Chen, Y.; Lin, Z. Barium titanate at the nanoscale: controlled synthesis and dielectric and ferroelectric properties. *Chemical Society Reviews* **2019,** *48* (4), 1194-1228.
(16) Liu, F.; Liu, Y.; Zhao, X.; Liu, X.; Fan, L.-Z. Pursuit of a high-capacity and long-life Mg-storage cathode by tailoring sandwich-structured MXene@ carbon nanosphere composites. *Journal of Materials Chemistry A* **2019**.
(17) Toby, B. H.; Von Dreele, R. B. GSAS-II: the genesis of a modern open-source all purpose crystallography software package. *Journal of Applied Crystallography* **2013,** *46* (2), 544-549.
(18) Lee, S. J.; Yang, H. M.; Cho, K. G.; Seol, K. H.; Kim, S.; Hong, K.; Lee, K. H. Highly conductive and mechanically robust nanocomposite polymer electrolytes for solid-state electrochemical thin-film devices. *Organic Electronics* **2019,** *65*, 426-433.
(19) Tabhane, G. H.; Giripunje, S. M.; Kondawar, S. B. Intensifying energy density, dielectric and mechanical properties of electroactive β-PVDF/f-BTO nanocomposites. *Physica B: Condensed Matter* **2019,** *571*, 149-161.
(20) Abbasipour, M.; Khajavi, R.; Yousefi, A. A.; Yazdanshenas, M. E.; Razaghian, F.; Akbarzadeh, A. Improving piezoelectric and pyroelectric properties of electrospun PVDF nanofibers using nanofillers for energy harvesting application. *Polymers for Advanced Technologies* **2019,** *30* (2), 279-291.

(21) Xu, L.; Li, G.; Guan, J.; Wang, L.; Chen, J.; Zheng, J. Garnet-doped composite polymer electrolyte with high ionic conductivity for dendrite-free lithium batteries. *Journal of Energy Storage* **2019,** *24*, 100767.
(22) Patel, S.; Kumar, R. Synthesis and characterization of magnesium ion conductivity in PVDF based nanocomposite polymer electrolytes disperse with MgO. *Journal of Alloys and Compounds* **2019,** *789*, 6-14.
(23) Morsi, M.; El-Khodary, S. A.; Rajeh, A. Enhancement of the optical, thermal and electrical properties of PEO/PAM: Li polymer electrolyte films doped with Ag nanoparticles. *Physica B: Condensed Matter* **2018,** *539*, 88-96.
(24) Ismail, A.; Mohammed, M.; Fouad, S. Optical and structural properties of polyvinylidene fluoride (PVDF)/reduced graphene oxide (RGO) nanocomposites. *Journal of Molecular Structure* **2018,** *1170*, 51-59.
(25) Nag, A.; Ali, M. A.; Singh, A.; Vedarajan, R.; Matsumi, N.; Kaneko, T. N-Boronated polybenzimidazole for composite electrolyte design of highly ion conducting pseudo solid-state ion gel electrolytes with a high Li-transference number. *Journal of Materials Chemistry A* **2019,** *7* (9), 4459-4468.
(26) Luo, J.; Li, Y.; Zhang, H.; Wang, A.; Lo, W.-S.; Dong, Q.; Wong, N.; Povinelli, C.; Shao, Y.; Chereddy, S. Metal-Organic Framework Thin Film for Selective Mg2+ Transport. *Angewandte Chemie International Edition*.
(27) Du, A.; Zhang, H.; Zhang, Z.; Zhao, J.; Cui, Z.; Zhao, Y.; Dong, S.; Wang, L.; Zhou, X.; Cui, G. A Crosslinked Polytetrahydrofuran-Borate-Based Polymer Electrolyte Enabling Wide-Working-Temperature-Range Rechargeable Magnesium Batteries. *Advanced Materials* **2019,** *31* (11), 1805930.
(28) Zhang, B.; Liu, Y.; Pan, X.; Liu, J.; Doyle-Davis, K.; Sun, L.; Liu, J.; Jiao, X.; Jie, J.; Xie, H. Dendrite-free lithium metal solid battery with a novel polyester based triblock copolymer solid-state electrolyte. *Nano Energy* **2020**, 104690.
(29) Luo, L.; Zhou, K.; Lian, R.; Lu, Y.; Zhen, Y.; Wang, J.; Mathur, S.; Hong, Z. Cation-Deficient TiO2 (B) Nanowires with Protons Charge Compensation for Regulating Reversible Magnesium Storage. *Nano Energy* **2020**, 104716.
(30) Kim, Y.-I.; Jung, J. K.; Ryu, K.-S. Structural study of nano BaTiO3 powder by Rietveld refinement. *Materials Research Bulletin* **2004,** *39* (7-8), 1045-1053.

Table of Contents graphic